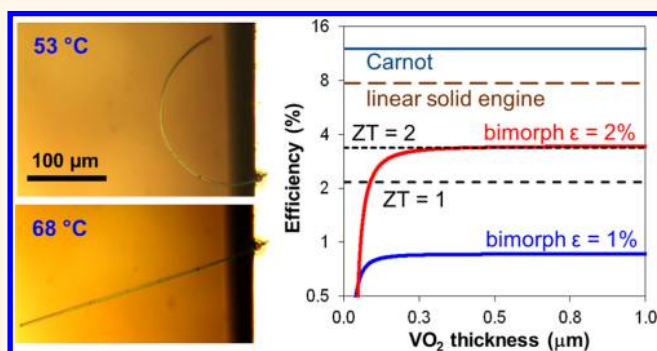


Performance Limits of Microactuation with Vanadium Dioxide as a Solid Engine

Kevin Wang,^{†,‡} Chun Cheng,^{†,‡} Edy Cardona,[†] Jingyang Guan,[†] Kai Liu,^{†,‡} and Junqiao Wu^{†,‡,*}

[†]Department of Materials Science and Engineering, University of California, Berkeley, California 94720, United States and [‡]Materials Sciences Division, Lawrence Berkeley National Laboratory, Berkeley, California 94720, United States

ABSTRACT Miniaturization of the steam engine to the microscale is hampered by severe technical challenges. Microscale mechanical motion is typically actuated with other mechanisms ranging from electrostatic interaction, thermal expansion, and piezoelectricity to more exotic types including shape memory, electrochemical reaction, and thermal responsivity of polymers. These mechanisms typically offer either large-amplitude or high-speed actuation, but not both. In this work we demonstrate the working principle of a microscale solid engine (μ SE) based on the phase transition of VO₂ at 68 °C with large transformation strain (up to 2%), analogous to the steam engine invoking large volume change in a liquid–vapor phase transition. Compared to polycrystal thin films, single-crystal VO₂ nanobeam-based bimorphs deliver higher performance of actuation both with high amplitude (greater than bimorph length) and at high speed (greater than 4 kHz in air and greater than 60 Hz in water). The energy efficiency of the devices is calculated to be equivalent to thermoelectrics with figure of merit $ZT = 2$ at the working temperatures, and much higher than other bimorph actuators. The bimorph μ SE can be easily scaled down to the nanoscale, and operates with high stability in near-room-temperature, ambient, or aqueous conditions. On the basis of the μ SE, we demonstrate a macroscopic smart composite of VO₂ bimorphs embedded in a polymer, producing high-amplitude actuation at the millimeter scale.



KEYWORDS: bimorph actuator · single-crystal · vanadium dioxide nanobeam · phase transition · microscale engine

Bilayer structures based on vanadium dioxide (VO₂) have demonstrated very large, reversible curvature changes when heated slightly above room temperature.^{1–3} VO₂ undergoes a first-order metal–insulator transition (MIT) at 68 °C, accompanied by a structural transition from a monoclinic phase (M1, $T < 68$ °C) to a tetragonal rutile phase (R, $T > 68$ °C) with a large transformation strain of $\sim 1\%$ along the rutile c -axis (c_R). Coupling VO₂ with an inactive material to form a bilayer structure enables actuation with giant amplitudes.² The transformation strain is several orders of magnitude higher than that of conventional bimorph actuators that rely on a difference in linear thermal expansion coefficient between two materials.⁴ Indeed, bimorphs incorporating polycrystal thin films of VO₂ on Si microcantilevers have achieved large curvature changes^{1,5} over 2500 m⁻¹, while

bimorphs utilizing single-crystal VO₂ nano/microbeams coupled with Cr have produced curvature changes³ over 23000 m⁻¹. Here, the single-crystalline nature of VO₂ nanobeams enhances the curvature change by aggregating the structural transformation strain along the bimorph length direction (nanobeam axis), in contrast to the case of polycrystal VO₂/Si where the strain is partially canceled and averaged along the bimorph length. This benefit results from the fact that single-crystal VO₂ nano/microbeams support single-domain MIT where the entire nano/microbeam cross section is a single structural phase, as opposed to spatially inhomogeneous MIT in the case of polycrystal VO₂ thin films.⁶ In addition to the large amplitude and high speed in actuation, the fact that the MIT in VO₂ can be triggered with a wide range of external stimuli (thermal, mechanical, and optical as well as electrical)^{1,7–9} greatly

* Address correspondence to wuj@berkeley.edu.

Received for review November 21, 2012 and accepted February 1, 2013.

Published online February 01, 2013
10.1021/nn305419e

© 2013 American Chemical Society

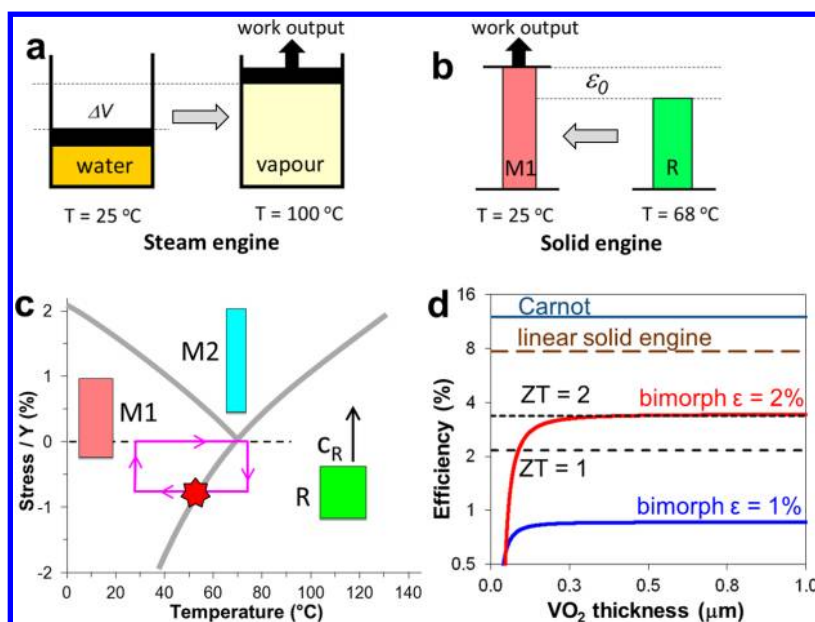


Figure 1. (a) Steam engine based on the liquid–vapor transition; (b) the microsolid engine based on a solid–solid phase transition; (c) the phase diagram (c_R stress vs temperature) of VO_2 . Here the stress is normalized by the Young's modulus (140 GPa), and positive (negative) means tension (compression). The three rectangular boxes show schematically the length of a VO_2 nanobeam in the three phases, where the length direction (c_R) is vertical. The rectangular loop shows a possible cycle of the solid engine, and the red star is the point where the work is done. (d) Calculated energy efficiency of a VO_2 -based linear solid engine and bimorph solid engines for transformation strain of $\varepsilon = 1\%$ (M1-R) and 2% (M2-R). Also shown is the energy efficiency of thermoelectrics with $ZT = 1$ and 2 , and the Carnot efficiency between 68 and 27 °C. Conventional bimorphs based on differential thermal expansion would have a negligibly low (0.002%) efficiency.

enriches the functionalities of such devices. However, the mechanism and fundamental limits of this VO_2 -based actuation technology have not been evaluated in terms of practical performance metrics such as energy efficiency, speed, and actuation amplitude.

In this work, we theoretically analyze and experimentally demonstrate these limits by investigating single-crystal VO_2 nanobeams side-coated with Cr as bimorph actuators in response to wind cooling as well as optical (laser) excitation. Here Cr is chosen for its high Young's modulus.² The devices actuate not only with larger amplitudes than those based on polycrystal VO_2 films, but also respond to optical activation deep into the kHz range, which is five times faster.¹⁰ A relatively high energy efficiency (equivalent to thermoelectrics of $ZT = 2.1$) is also predicted. By varying the frequency and location of the laser excitation, we analyze the heat transfer dynamics in these structures. The bending state of the thermally actuated device depends on the phase composition and domain structure of VO_2 , which is dictated by the temperature profile along the bimorph. Thus, the ability of the cantilevered bimorph to accumulate and dissipate heat determines the maximum frequency at which such an actuator can be operated. Bimorph cantilevers with submicrometer cross sections exhibit enhanced rates of heat dissipation to ambient air benefiting from their large surface to volume ratio,¹¹ and thus deliver actuation at higher speed compared to their thin-film based counterparts with bimorph widths far above micrometers.

RESULTS AND DISCUSSION

High Energy Efficiency of Actuation. Figure 1 panels a and b show the analogy between the proposed microscale solid engine (μSE) and the steam engine. It is known that the size change from a solid–solid structural transition is much smaller than the volume expansion in the liquid–vapor transition. However, solids offer much stronger force, which compensates for the small displacement. VO_2 is such a solid and undergoes the transition at 68 °C. Compared to the M1 structure, the R structure shrinks along the c_R -axis by $\sim 1\%$ and expands along the other two directions.¹² A second monoclinic, insulating phase (M2) can be stabilized by doping^{13–15} or tensile stress^{16–18} along c_R , as shown in the phase diagram¹⁹ in Figure 1c. The M2 phase, on the other hand, elongates by about 1% along c_R compared to M1.²⁰ The strain is thus $\sim 2\%$ between the M2 and R phases.

In microactuation, high amplitude and high force tend to be mutually exclusive due to the limited output work density of the working material that drives the actuation. The volumetric work density describes maximum mechanical work output per unit volume of the working material. It is given by $Y\varepsilon^2/2$, where Y is the Young's modulus of the material, which determines the amount of force, and ε is its maximum strain, which limits the actuation amplitude. The work density of VO_2 was estimated to be 0.63 J/cm^3 for polycrystal films.² This value is calculated to be 7 J/cm^3 for single-crystal VO_2 beams, which is comparable to shape memory

alloys, more than 10 times higher than that of most organic materials and electrostrictive polymers, hundreds of times higher than piezoresistive materials,²¹ and 3 orders of magnitude higher than human muscles.

The theoretical energy efficiency of a single-crystal VO₂ nano/microbeam oriented along c_R as a linear μ SE can be calculated by dividing the maximum work output from the axial elongation by the total heat needed to drive the MIT. The former is calculated from the critical stress across the MIT, which is related to the latent heat (H) through the Clapeyron equation.⁶ The latter is the sum of the latent heat and the energy needed to heat the VO₂ from $T_{\text{low}} = 27$ °C to $T_{\text{high}} = 68$ °C. The efficiency is found to be (see Supporting Information),

$$\eta_{\text{linear}} = \frac{T_{\text{high}} - T_{\text{low}}}{T_{\text{high}}} \frac{1}{1 + c\rho \cdot (T_{\text{high}} - T_{\text{low}})/H} \quad (1)$$

where c is the specific heat and ρ is the density of VO₂. Equation 1 highlights that a higher latent heat for the phase transition results in a higher efficiency, being utilized to output work through the material expansion, while the specific heat contributes to heating the working material and represents a loss in the energy efficiency. A possible thermodynamic cycle for the μ SE is illustrated in Figure 1c, with work being output as the VO₂ cools and expands from the R phase to M1 phase. Figure 1d shows a high efficiency of 7.7%, equal to 64% of the Carnot efficiency (12%) for a linear μ SE operating between 27 and 68 °C. However, the displacement needs to be magnified for practical use. We couple the VO₂ nanobeam with a clamping layer (Cr in this case) forming a bimorph μ SE to offer large microscale actuation transverse to the nanobeam axis (Figure 2 panels a and b).

By treating the bimorph as an elastic bilayer beam with a spring constant, we can calculate its energy efficiency as a function of VO₂ thickness for $\varepsilon = 1\%$ (M1-R) and 2% (M2-R). An efficiency of $\sim 3.4\%$ is predicted for VO₂/Cr nanobeam bimorphs involving the M2-R transition (see Supporting Information). Impressively, this is equivalent in efficiency to thermoelectrics with figure-of-merit $ZT = 2.1$ operating between these two temperatures. As another comparison, conventional bimorphs based on differential thermal expansion between the two layers over this temperature range are estimated to have a much lower energy efficiency of $\sim 0.002\%$.

The transformation strain, 1% for M1-R and 2% for the M2-R transition, is not only several orders of magnitude higher than that of conventional inorganic bimorph actuators relying on differential thermal expansion,⁴ but also much higher than the saturation strain in piezoelectric materials. Finally, shape memory alloys²² and organics-based actuators²³ may provide strains greater than 5%, but VO₂ maintains the

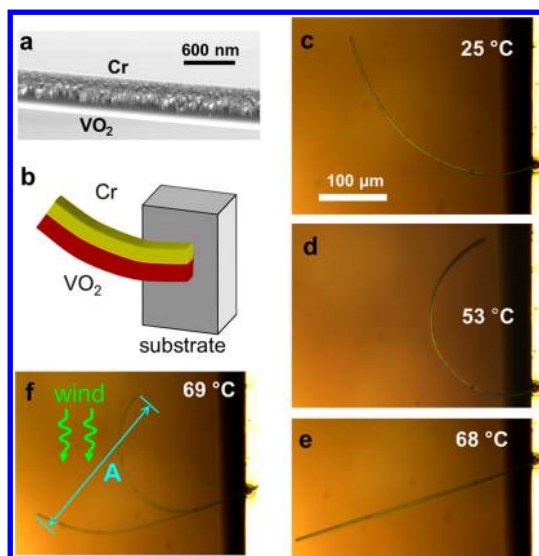


Figure 2. (a) A close-up scanning electron microscopy image of the VO₂/Cr bimorph; (b) schematic of a VO₂/Cr bimorph cantilevered from the substrate; (c,d,e) optical image of a cantilevered VO₂(1 μ m)/Cr(0.3 μ m) bimorph at substrate temperature of 25, 53, and 68 °C; length $L = 217$ μ m and width $a = 1$ μ m; (f) fast and high-amplitude oscillation of the bimorph under room-temperature wind cooling where the substrate is at 69 °C.

advantage of much higher force (due to higher Young's modulus) and speed (due mostly to lower temperature change needed).

High-amplitude actuation activated by global heating/cooling. Single-crystal VO₂ nanobeams grown by vapor transport are always oriented along the c_R direction with a rectangular cross section.²⁴ In a cantilevered bimorph of a VO₂ nanobeam coupled with Cr (Figure 2a), the VO₂ near the interface is typically under compressive stress at room temperature, and the bimorph bends into a high curvature state toward the Cr side (Figure 2c). In heating the device above 68 °C, the VO₂ contracts into the R phase and the bimorph straightens, as shown in Figure 2e. We define the actuation amplitude, A , to be the linear tip displacement between these two bimorph configurations. The normalized amplitude between these two states, A divided by the bimorph length L , is typically $A/L \sim 0.8$ or higher. This amplitude is extraordinarily large compared to inorganic bimorphs based on other mechanisms, and is also greater by nearly a factor of 3 than that achieved in polycrystal VO₂/Si bimorphs.^{1,5} The actuation can be induced by global (*i.e.*, substrate) heating as in this case, but it can be also activated by environmental temperature fluctuation (*e.g.*, wind), as well as by local heating (*e.g.*, a focused laser).

When heating the Si substrate to above 68 °C and simultaneously blowing gentle, room-temperature wind toward the device, the VO₂/Cr bimorph cantilevers rapidly and irregularly oscillate (Figure 2f and video in Supporting Information). The oscillation arises from turbulent air convection that cools the bimorph

cantilever across the MIT, rather than any mechanical pushing force imposed by the wind. To confirm this, we performed the same experiment without heating the Si substrate, and the VO₂/Cr cantilever did not oscillate with any speed or direction of wind. This is expected because the kinetic force from the wind onto objects with submicrometer cross section is negligible.

Upon global heating, the bimorphs bend outward (straightening) at $T > 68$ °C as expected for the M1-R transition; interestingly, before that, at intermediate temperatures, the VO₂ bimorphs bend inward (increasing curvature, Figure 2d). Due to the ~1% elongation of the VO₂ nanobeam upon the M1–M2 phase transition, the VO₂/Cr bimorph bends further toward the Cr side resulting in an increase in curvature. This strain is more than an order of magnitude higher than the contribution of linear thermal expansion difference^{12,25} between Cr and VO₂, which produces a strain of only 0.028% between room temperature and 68 °C. This M2 strain also significantly increases the actuation amplitudes, with A/L rising to >1.2 in most bimorphs. This is analyzed below in more detail using local laser heating.

Spatially Resolved Activation by Local Heating with a Focused Laser. A laser focused on the VO₂/Cr bimorph thermally actuates the device by locally driving the phase transition at the hot spot along the VO₂ nanobeam. The dynamics of heat transfer for our quasi-1D system are governed by^{11,26}

$$\rho c \frac{\partial T(x, t)}{\partial t} = \kappa \frac{\partial^2 T(x, t)}{\partial x^2} - 2h \frac{a+b}{ab} [T(x, t) - T_0] \quad (2)$$

where κ is the effective thermal conductivity of the nanobeam bimorph, T_0 is the environment temperature (27 °C), h is the total heat transfer coefficient from the bimorph surface to air, and a and b are the bimorph width and thickness, respectively. In the case of continuous local laser heating at a fixed location, varying laser power produces different bending curvatures as shown in Figure 3. We attribute the inward (outward) bending to the laser activated local transition of M1 to M2 (R). This is further confirmed by μ -Raman spectroscopy carried out at different laser intensities. The Raman spectrum recorded at the intermediate (high) laser intensities clearly proves the local emergence of the M2 (R) phase. We note that in bimorphs based on polycrystal VO₂ thin films, due to their spatially inhomogeneous phase transition, such clear M1-M2-R transition and the resultant amplitude enhancement are not resolved.^{1,5}

By investigating the bimorph bending as a function of continuous laser power and focusing position, we obtain a clear picture of the actuation behavior. As shown in Figure 4a, for a fixed laser position, low to intermediate laser powers cause the bimorph to deflect in the negative direction (bending inward) due to the M1-M2 transition, while high laser powers produce

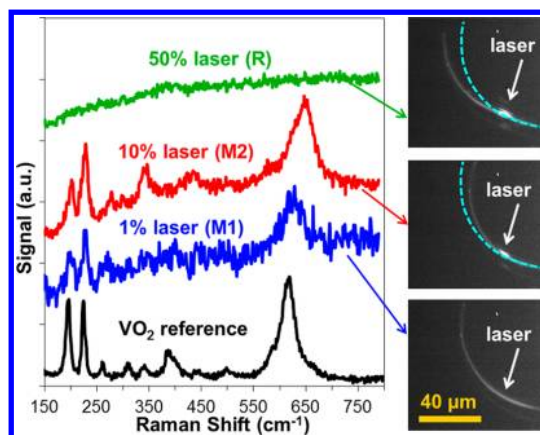


Figure 3. Three bending states of a VO₂/Cr bimorph activated by a continuous laser heating at increasing laser intensities (1%, 10%, and 50%), corresponding to M1, M2, and R local phase at the laser spot as identified by the Raman spectra. It is known that the 615 cm⁻¹ peak in the M1 phase shifts to 650 cm⁻¹ in the M2 phase,^{29,30} and the R phase exhibits no Raman due to its metallicity. The dashed curve in two of the images represents the original bimorph configuration to show the bending. The experiments were performed in ambient and the substrate is at room temperature. Here 100% laser power corresponds to 1 mW.

deflection in the positive, outward direction due to the M1-R transition. The temperature distribution depends primarily on heat dissipation through two channels: (i) “sub”, conduction along the bimorph to the Au/Si substrate, and (ii) “air”, dissipation to the ambient *via* air convection and conduction, as shown in the first and second terms on the right-hand side in eq 2. The characteristic time constants for these two heat dissipation channels²⁶ are $\tau_{\text{sub}} = x^2 \rho c / 4\kappa$ and $\tau_{\text{air}} = (\rho c / h) \cdot ab / (a + b)$. It is immediately seen that τ_{sub} depends only upon the distance (x) for heat to diffuse from the laser spot to the substrate, while τ_{air} relies only on the bimorph surface area in contact with air. For typical devices at laser position $x \approx 150$ μm , we estimate the characteristic maximum response frequencies to be $f_{\text{sub}} = 1/\tau_{\text{sub}} \approx 0.4$ kHz, and $f_{\text{air}} = 1/\tau_{\text{air}} \approx 3$ kHz. We also note that bimorphs with smaller cross section would perform well up to higher frequencies, owing simply to the higher surface-to-volume ratio which reduces τ_{air} . Figure 4b displays the x -dependence of bimorph bending angle between laser on and off (in the low-frequency limit), calculated from $\theta \approx A/(L - x)$. Approaching the root ($x = 0$), the rapid drop in θ is due to the increasing “sub” effect. Far from the root and the substrate, the x -independent “air” effect dominates as expected.

High-Speed Operation and Frequency Dependence. For many applications, it is critically important for the actuator to operate at high speed. We now activate the actuation with pulsed localized heating by chopping the incident laser beam at frequency f . At very high frequencies, the actuation amplitude A is expected to rapidly decrease, due to inability of the bimorph to dissipate heat and

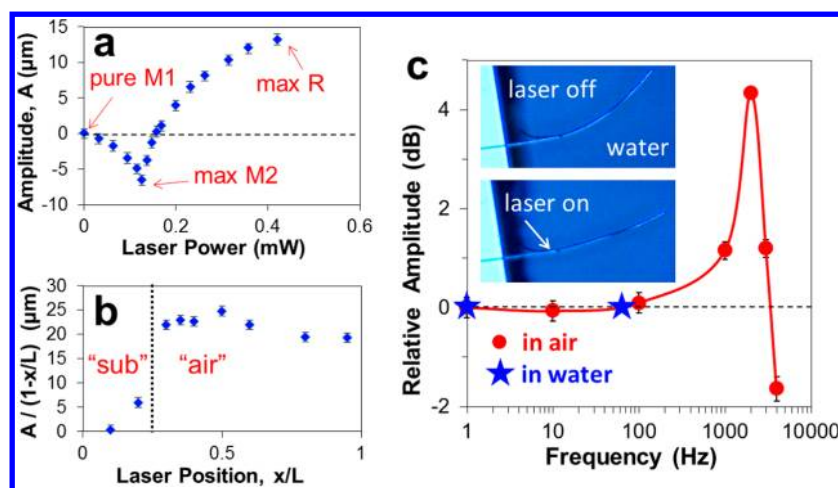


Figure 4. (a) Actuation amplitude as a function of continuous laser power at fixed laser position $x/L = 0.3$. Negative amplitude indicates inward bending due to the activation of M2 phase. (b) $L \cdot \theta$ as a function of laser position at fixed laser power of 0.4 mW, where $\theta \approx A/(L - x)$ is the bending angle. Here the bimorph is $\text{VO}_2(700 \text{ nm})/\text{Cr}(200 \text{ nm})$, length $L = 100 \mu\text{m}$, width $a = 700 \text{ nm}$, and the substrate is at room temperature. (c) Amplitude of actuation operated in room air and water activated with a chopped laser. Here the bimorph is $\text{VO}_2(900 \text{ nm})/\text{Cr}(300 \text{ nm})$, length $L = 115 \mu\text{m}$, width $a = 900 \text{ nm}$. Incident laser power is 0.5 mW and relative position is fixed at $x/L = 0.5$. Inset shows actuation in deionized water with a continuous laser.

return to its original unheated state within the period of time $1/f$. From bimorphs based on polycrystal VO_2 films, Merced *et al.*¹⁰ observed the attenuation of A to -3 dB ($1/\sqrt{2}$ amplitude) at a laser chopping frequency $f_{-3\text{dB}} \approx 1 \text{ kHz}$. Figure 4c shows measured A versus f from a typical nanobeam VO_2/Cr bimorph. Here we plot $A(f)$ in decibels by $20 \cdot \log[A(f)/A_{\text{DC}}]$, where $A_{\text{DC}} = A(f = 0)$ is the linear displacement of the bimorph tip between its unperturbed position and its state under continuous laser activation (with the same laser intensity). It can be seen that indeed for very high frequencies ($f > \sim 3 \text{ kHz}$), A starts to decrease; but at intermediate frequencies, A actually increases. This is because the VO_2 nanobeam at the laser spot is no longer just switching between M1 and R phases with 1% axial strain, but is instead transitioning between M2 and R phases with higher ($\sim 2\%$) axial strain.

The phase diagram in Figure 1c helps clarify the behavior at intermediate frequencies, where the bimorph loop is raised upward and right into the M2/R region. Now, the useful work could be collected at the M2 phase boundary, while cooling limitations prevent the VO_2 from switching back to the M1 state. To ensure that the rise in amplitude is not due to mechanical resonance, the cantilever's resonant frequency was calculated (Supporting Information) to be 1.29 MHz, significantly higher than the optical actuation frequencies. At the maximum laser chopping frequency of 4 kHz, A has dropped to only about -2 dB . Extrapolating the data points beyond here, we estimate the 3 dB-attenuation frequency of $f_{-3\text{dB}}$ is $\sim 4.5 \text{ kHz}$, nearly five times faster than values reported for bimorphs with polycrystal VO_2 films.⁵ This is expected from the much smaller cross section of our bimorphs and is consistent with the f_{air} estimated above.

Operation in Aqueous Condition. In addition to working in air, the nanobeam device also delivers high-

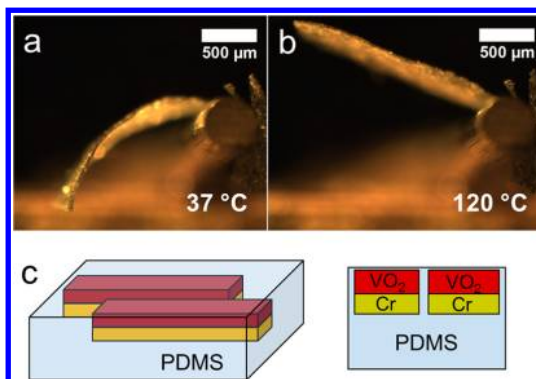


Figure 5. (a) Low-temperature curved state of the hybrid smart composite film; (b) high-temperature straightened state. Global heating is provided through the metal base at the right. The film is 2 mm long, 1 mm wide, and $20 \mu\text{m}$ thick. (c) Schematic 3D view and cross section view of the hybrid composite film.

amplitude and high-speed actuation in aqueous conditions. The inset of Figure 4c shows the bimorph deflected by a laser in water. From the recorded video (Supporting Information), the actuation is stable and the response time in water is faster than 17 ms, the time resolution of our camera. This is faster by several orders of magnitude than other aqueous actuation mechanisms such as polymer swelling. Compared to polymeric materials, the higher speed arises fundamentally from the much higher thermal conductivity and lower specific heat of VO_2 , as well as the fast speed of the MIT and the small temperature rise needed to drive the MIT.

Demonstration of a Hybrid Smart Composite. By aligning VO_2/Cr bimorphs and incorporating them into a polymer matrix, we can extend the large-amplitude actuation to the macro-scale, and form a hybrid smart composite film, useful for fluidic valves and smart

shape-programmable structures. Figure 5 shows the large-amplitude actuation ($A/L = 0.9$) by globally heating such a millimeter-scale smart composite. The composite is a dense assembly of aligned VO_2/Cr bimorphs embedded into a thin film of polydimethylsiloxane (PDMS) measuring $2 \text{ mm} \times 1 \text{ mm}$ in size. A slight inward bending was also observed between 25 and 37 °C, consistent with the M2 phase formation in VO_2 . It can be envisioned that by depositing Cr onto only patterned regions of aligned VO_2 nanobeams, followed by PDMS molding, one can program the location, direction, and amplitude of actuation in the smart composite.

CONCLUSION

We report a bimorph actuator composed of a single-crystal VO_2 nanobeam coupled with a Cr layer. Unlike traditional bimorph actuators based on differential thermal expansion, the actuation of this device is activated upon the structural phase transition in VO_2 at a temperature slightly above room temperature. The actuation can be driven thermally, photothermally, or electrically. We investigate time-independent and time-dependent actuation behavior of the actuators using focused pulsed laser heating. Compared to previously reported bimorph actuators based on polycrystal VO_2 thin films with much larger width, these single-crystal VO_2 nanobeam-based bimorphs exhibit superior performance in terms of (i) much higher actuation amplitude (by a factor of ~ 3), and (ii) much faster

response speed (by five times). The former is explained by the single-crystallinity of the VO_2 nanobeam used, such that the VO_2 undergoes the phase transition *via* a single domain to maximize the use of transformation strain, as opposed to random, multiple domains in the case of thin films. The latter is explained by the smaller width and thus higher surface-to-volume ratio of a nanobeam-based bimorph, which facilitates heat dissipation to ambient air. Moreover, due to the single-domain nature of the phase transition, an otherwise hidden phase (M2) plays an important role; a complicated and nonmonotonic actuation behavior is observed and explained on the basis of the phase diagram of VO_2 . The energy efficiency of our devices is calculated to be equivalent to thermoelectrics with $ZT = 2.1$.

The bimorph as a μSE can be easily fabricated and integrated at the nanoscale and up to the macroscale. The device functions may be further broadened and efficiency further enhanced by reducing the MIT temperature of VO_2 from 68 °C toward room temperature with a small concentration of tungsten doping.²⁷ As heat slightly above room temperature is ubiquitous and much more abundant than those at higher temperatures, the bimorph μSE demonstrated here may be used as sensors, actuators, and energy harvesters operating in near-room-temperature, ambient or aqueous conditions, including physiological and microfluidic environments.

METHODS

Nanobeam Growth. Ultralong VO_2 nanobeams were synthesized in a horizontal tube furnace from V_2O_5 powder (99%, Sigma-Aldrich), following a recently reported vapor transport method.²⁸ Unpolished quartz substrates were placed downstream from the source powder, resulting in long, freestanding nanobeams. The growth conditions were as follows: temperature ≈ 880 °C, Ar carrier gas pressure ≈ 5 Torr, flow rate ≈ 7 sccm, and time ≈ 3 h. The growth products were analyzed by Raman and heated optical microscopy to confirm the identity and phase transition properties.

Bimorph Cantilever Preparation. Nanobeams were manually transferred into the edge of Si substrates (Si substrate was precoated with 10 nm Cr and then 300 nm Au to enhance thermal conductivity). Next, the nanobeams were clamped onto these substrates through ion-beam induced Pt deposition, with Pt thickness roughly matching the nanobeam thickness to ensure sufficient clamping and thermal conductivity. Next, a layer of Cr was deposited onto the side of the VO_2 cantilevers by electron-beam evaporation. Here Cr is chosen for its high Young's modulus. A Cr/ VO_2 thickness ratio of ~ 0.4 was used to maximize the bending curvature, calculated from beam bending theory.³ Finally, the bilayer cantilevers were annealed in Ar at 250 °C to improve the clamping between Cr and VO_2 .

Hybrid Film Fabrication. Long and free-standing nanobeams grown on unpolished quartz were brushed several times with a Si chip to flatten and roughly align in the desired actuation direction. Next, bimorphs were formed by e-beam evaporation of Cr. PDMS (10:1 monomer ratio) was dropcast onto a heated bimorph chip (85 °C) so that the bimorphs are all straight. The chip was spun at 7000 rpm for 45 s and quickly returned to the

hot plate for curing at 85 °C for 4 h . Finally, the film was cut with a scalpel and peeled with a probe tip.

Laser Actuation. A continuous-wave argon ion laser (514.5 nm) provided local heating to nanobeam cantilevers at room temperature. A low-jitter optical chopper pulsed the laser up to 4 kHz . A CCD video camera captured the fast oscillation of the cantilevers, and the tip moving amplitudes were extracted from individual video frames. We note that our camera is not fast enough to resolve each position of the bimorph oscillating at high frequencies, but the oscillation amplitude can be clearly determined from the video frames.

Raman Characterization. Micro-Raman spectroscopy was conducted at room temperature using a Renishaw 2600 system, with excitation provided by a 488 nm Ar-ion laser. An Olympus $50\times$ objective was used and the Raman signal was collected for several minutes, with laser intensities tuned to produce desired amounts of bending.

Conflict of Interest: The authors declare no competing financial interest.

Acknowledgment. K. W. was supported by the National Science Foundation under Grant No. EEC-0832819 through the Center of Integrated Nanomechanical Systems. Materials preparation and device fabrication were supported by the National Science Foundation under Grant No. ECCS-1101779. We are grateful for permission to use the laser setup in Prof. C. P. Grigoropoulos's lab, as well as assistance from Richard Novak and Lakshmi Jagannathan.

Supporting Information Available: Movies of actuation by wind, high and low frequency laser, and self-oscillation under continuous laser; additional actuation frequency data and

theoretical efficiency analysis. This material is available free of charge via the Internet at <http://pubs.acs.org>.

REFERENCES AND NOTES

- Rua, A.; Fernandez, F. E.; Sepulveda, N. Bending in VO₂-coated Microcantilevers Suitable for Thermally Activated Actuators. *J. Appl. Phys.* **2010**, *107*, 074506.
- Liu, K.; Cheng, C.; Cheng, Z.; Wang, K.; Ramesh, R.; Wu, J. Giant-Amplitude, High-Work Density Microactuators with Phase Transition Activated Nanolayer Bimorphs. *Nano Lett.* **2012**, *12*, 6302–6308.
- Cao, J.; Fan, W.; Zhou, Q.; Sheu, E.; Liu, A.; Barrett, C.; Wu, J. Colossal Thermal-Mechanical Actuation via Phase Transition in Single-Crystal VO₂ Microcantilevers. *J. Appl. Phys.* **2010**, *108*, 083538.
- Toda, M.; Ono, T.; Liu, F.; Voiculescu, I. Evaluation of Bimaterial Cantilever Beam for Heat Sensing at Atmospheric Pressure. *Rev. Sci. Instrum.* **2010**, *81*, 055104.
- Cabrera, R.; Merced, E.; Sepúlveda, N.; Fernández, F. E. Dynamics of Photothermally Driven VO₂-Coated Microcantilevers. *J. Appl. Phys.* **2011**, *110*, 094510.
- Cao, J.; Ertekin, E.; Srinivasan, V.; Fan, W.; Huang, S.; Zheng, H.; Yim, J. W. L.; Khanal, D. R.; Ogletree, D. F.; Grossman, J. C.; *et al.* Strain Engineering and One-Dimensional Organization of Metal-Insulator Domains in Single-Crystal Vanadium Dioxide Beams. *Nat. Nanotechnol.* **2009**, *4*, 732–737.
- Strelcov, E.; Lilach, Y.; Kolmakov, A. Gas Sensor Based on Metal-Insulator Transition in VO₂ Nanowire Thermistor. *Nano Lett.* **2009**, *9*, 2322–2326.
- Tselev, A.; Budai, J. D.; Strelcov, E.; Tischler, J. Z.; Kolmakov, A.; Kalinin, S. V. Electromechanical Actuation and Current-Induced Metastable States in Suspended Single-Crystalline VO₂ Nanoplatelets. *Nano Lett.* **2011**, *11*, 3065–3073.
- Sengupta, S.; Wang, K.; Liu, K.; Bhat, A. K.; Dhara, S.; Wu, J.; Deshmukh, M. M. Field-Effect Modulation of Conductance in VO₂ Nanobeam Transistors with HfO₂ as the Gate Dielectric. *Appl. Phys. Lett.* **2011**, *99*, 062114.
- Merced, E.; Dávila, N.; Torres, D.; Cabrera, R.; Fernández, F. E.; Sepúlveda, N. Photothermal Actuation of VO₂-Cr-coated Microcantilevers in Air and Aqueous Media. *Smart Mater. Struct.* **2012**, *21*, 105009.
- Cheng, C.; Fan, W.; Cao, J.; Ryu, S.-G.; Ji, J.; Grigoropoulos, C. P.; Wu, J. Heat Transfer Across the Interface between Nanoscale Solids and Gas. *ACS Nano* **2011**, *5*, 10102–10107.
- Kucharczyk, D.; Niklewski, T. Accurate X-ray Determination of the Lattice Parameters and the Thermal Expansion Coefficients of VO₂ Near the Transition Temperature. *J. Appl. Crystallogr.* **1979**, *12*, 370–373.
- Marezio, M.; McWhan, D. B.; Remeika, J. P.; Dernier, P. D. Structural Aspects of the Metal-Insulator Transitions in Cr-Doped VO₂. *Phys. Rev. B* **1972**, *5*, 2541–2551.
- Rua, A.; Cabrera, R.; Coy, H.; Merced, E.; Sepulveda, N.; Fernandez, F. E. Phase Transition Behavior in Microcantilevers Coated with M1-phase VO₂ and M2-phase VO₂:Cr Thin Films. *J. Appl. Phys.* **2012**, *111*, 104502.
- Zhang, S.; Kim, I. S.; Lauthon, L. J. Stoichiometry Engineering of Monoclinic to Rutile Phase Transition in Suspended Single Crystalline Vanadium Dioxide Nanobeams. *Nano Lett.* **2011**, *11*, 1443–1447.
- Tselev, A.; Strelcov, E.; Luk'yanchuk, I. A.; Budai, J. D.; Tischler, J. Z.; Ivanov, I. N.; Jones, K.; Proksch, R.; Kalinin, S. V.; Kolmakov, A. Interplay between Ferroelastic and Metal-Insulator Phase Transitions in Strained Quasi-Two-Dimensional VO₂ Nanoplatelets. *Nano Lett.* **2010**, *10*, 2003–2011.
- Guo, H.; Chen, K.; Oh, Y.; Wang, K.; Dejoie, C.; Syed Asif, S. A.; Warren, O. L.; Shan, Z. W.; Wu, J.; Minor, A. M. Mechanics and Dynamics of the Strain-Induced M1–M2 Structural Phase Transition in Individual VO₂ Nanowires. *Nano Lett.* **2011**, *11*, 3207–3213.
- Okimura, K.; Watanabe, T.; Sakai, J. Stress-Induced VO₂ Films with M2 Monoclinic Phase Stable at Room Temperature Grown by Inductively Coupled Plasma-Assisted Reactive Sputtering. *J. Appl. Phys.* **2012**, *111*, 073514.
- Cao, J.; Gu, Y.; Fan, W.; Chen, L. Q.; Ogletree, D. F.; Chen, K.; Tamura, N.; Kunz, M.; Barrett, C.; Seidel, J.; *et al.* Extended Mapping and Exploration of the Vanadium Dioxide Stress-Temperature Phase Diagram. *Nano Lett.* **2010**, *10*, 2667–2673.
- Brückner, W. Structural Relations between the VO₂ Phases. *Krist. Tech.* **1981**, *16*, K28–K31.
- Steeneken, P. G.; Phan, K. L.; Goossens, M. J.; Koops, G. E. J.; Brom, G. J. a. M.; van der Avoort, C.; Beek, J. T. M. Piezoresistive Heat Engine and Refrigerator. *Nat. Phys.* **2011**, *7*, 354–359.
- Liu, Y. The Work Production of Shape Memory Alloy. *Smart Mater. Struct.* **2004**, *13*, 552–561.
- Lima, M. D.; Li, N.; de Andrade, M. J.; Fang, S.; Oh, J.; Spinks, G. M.; Kozlov, M. E.; Haines, C. S.; Suh, D.; Foroughi, J.; *et al.* Electrically, Chemically, and Photonically Powered Torsional and Tensile Actuation of Hybrid Carbon Nanotube Yarn Muscles. *Science* **2012**, *338*, 928–932.
- Wu, J.; Gu, Q.; Guiton, B. S.; de Leon, N. P.; Ouyang, L.; Park, H. Strain-Induced Self Organization of Metal-Insulator Domains in Single-Crystalline VO₂ Nanobeams. *Nano Lett.* **2006**, *6*, 2313–2317.
- Koumelis, C. N. The Thermal Expansion Coefficient of Chromium in the Temperature Region of 3 to 80 °C. *Phys. Stat. Sol.* **1973**, *19*, K65–K69.
- Incropera, F. P.; DeWitt, D. P. *Introduction to Heat Transfer*; John Wiley & Sons: New York, 2002; pp 516–518.
- Gu, Q.; Falk, A.; Wu, J.; Ouyang, L.; Park, H. Current-Driven Phase Oscillation and Domain-Wall Propagation in W₂V_{1-x}O₂ Nanobeams. *Nano Lett.* **2007**, *7*, 363–366.
- Cheng, C.; Liu, K.; Xiang, B.; Suh, J.; Wu, J. Ultra-Long, Free-Standing, Single-Crystalline Vanadium Dioxide Micro/Nanowires Grown by Simple Thermal Evaporation. *Appl. Phys. Lett.* **2012**, *100*, 103111.
- Atkin, J. M.; Berweger, S.; Chavez, E. K.; Raschke, M. B.; Cao, J.; Fan, W.; Wu, J. Strain and Temperature Dependence of the Insulating Phases of VO₂ near the Metal-Insulator Transition. *Phys. Rev. B* **2012**, *85*, 020101.
- Tselev, A.; Luk'yanchuk, I. A.; Ivanov, I. N.; Budai, J. D.; Tischler, J. Z.; Strelcov, E.; Kolmakov, A.; Kalinin, S. V. Symmetry Relationship and Strain-Induced Transitions between Insulating M1 and M2 and Metallic R Phases of Vanadium Dioxide. *Nano Lett.* **2010**, *10*, 4409–4416.

Performance Limits of Micro-Actuation with Vanadium Dioxide as a Solid Engine

Kevin Wang, Chun Cheng, Edy Cardona, Jingyang Guan, Kai Liu, Junqiao Wu

1. Wind actuation (Movie 1).

Video of the bimorph actuation via wind cooling is shown in Movie 1. Here, the substrate is heated to 69 °C, and 500 sccm of wind is directed in a direction opposite to the bimorph bending (inwards, increasing curvature). The observed bending amplitude is very large ($A/L \sim 0.8$), but the duty cycle is moderate to low (< 50%).

At higher substrate temperatures, the VO_2/Cr bimorph becomes increasingly difficult to cool across the metal-insulator phase transition (MIT), resulting in smaller amplitude in oscillation. Increasing wind speed does not increase the amplitude greatly, but it noticeably increases the oscillation duty cycle. That is, for any given period of observation time, stronger wind causes more instances of bimorph actuation and lowers the time percentage that the bimorph stays stationary. The duty cycle is characterized as low, medium, or high depending on the percentage of times the bimorph is oscillating between the straight and bent states, as observed in the videos collected. The results of these trials at substrate temperatures of 68 and 75 °C for 3 different wind speeds are listed in Tab. S1.

Substrate Temperature	Wind Flow (sccm)	Nominal amplitude (μm)	Oscillation Duty Cycle
68 °C	200	230	Low
	500	238	Medium
	2000	235	Medium
75 °C	200	206	Low
	500	181	Medium
	2000	201	High

Tab. S1. Bending amplitude and qualitative switching duty of a cantilevered bimorph under various wind flow rates and two substrate temperatures. The bimorph is $\text{VO}_2(1 \mu\text{m})/\text{Cr}(0.3 \mu\text{m})$ with length $L = 217 \mu\text{m}$ and width $a = 1 \mu\text{m}$. Amplitude error is $\pm 5 \mu\text{m}$.

2. Laser actuation in water (Movie 2).

Movie 2 shows the bending of a bimorph soaked in de-ionized water and activated with a laser beam turned repeatedly on and off. By analyzing individual video frames, it is found that the bimorph completes bending within the time lapse between two consecutive frames. The

video frame rate is 60/sec, giving an upper limit of the response time of ~17 msec and lower frequency limit of 60Hz. The actual speed should be much faster.

The amplitude response of the device shown is much lower than that shown in the main text, Fig. 4c, due to the illumination point far from the base, exciting a reduced region to phase transition. Additionally, the Cr has started delaminating, visibly peeling from the base of the bimorph and causing discontinuities along the bimorph length. The loss of bonding between the two layers dramatically reduces the net strain difference in the bimorph, reducing the amplitude change. Physical degradation like this can be prevented by a more careful Cr deposition, followed by a post-deposition anneal.

3. Nucleation of the M2 phase at intermediate temperatures.

From the strain-temperature phase diagram (Fig.1c), we expect the M2 phase to be stable at intermediate temperatures under tensile strain. We attribute the nucleation of M2 in the bimorphs to be at the free side of the curved VO₂ nanobeam, which is under tensile strain. Cr diffusion into VO₂ at the VO₂/Cr interface also tends to stabilize the M2 structure,¹ but this is unlikely the leading effect here, since the Cr deposition and rapid anneal at 250 °C is not expected to diffuse much Cr into the VO₂ nanobeam.

4. Pulsed laser actuation (Movie 3, Movie 4).

The bimorph actuation can be analyzed by decomposing the total oscillation amplitude into inward bending amplitude A^{M2} (from the unperturbed position towards the max M2 position) and outward bending amplitude A^R (from the unperturbed position towards the max R position), so that the total amplitude $A(f) = A^{M2}(f) + A^R(f)$. By plotting the two oscillation amplitudes separately, we see that the rise in $A(f)$ at intermediate f results from an increase in $A^{M2}(f)$, as shown in Fig. S1. This is explained by the limited cooling as the frequency rises. The peaking and eventual decrease of $A^{M2}(f)$ at higher f also occur due to the cooling limitations – the VO₂ is unable to cool to a sufficiently low temperature, not even able to reach the M2 phase, and therefore stays in the heated R phase during the entire time of laser pulsing. The results with varying frequency at 3 positions along this bimorph are shown in Fig. S1. A sustained outward bending behavior can be seen for $x/L = 0.3$, producing considerable bending up to high frequencies. The high performance may represent an optimal excitation position on this bimorph, maximizing both “sub” and “air” modes of heat transfer and increasing the operating speed of the device.

By comparing the $A(f)$ dependence between bimorphs of various cross section areas, we can better understand the “air” term of heat dissipation. Figure S2 plots $A(f)$ for 3 bimorphs and reveals an improving high-frequency performance as the VO₂ thickness decreases. The peak displacements occur at frequencies of ~ 1, 2, and 3 kHz for bimorphs with VO₂ nanobeam thickness of 1, 0.9 and 0.7 μm respectively. This agrees with the predicted behavior, since the thinner bimorph has a greater surface to volume ratio, which increases the efficacy of the heat dissipation to air. Referring to the time constant τ_{air} in the main text, the characteristic frequency

is inversely proportional to the “effective bimorph diameter”, $ab/(a + b)$. This qualitatively agrees with our observation of higher $f_{-3\text{dB}}$ at smaller bimorph thickness.

Due to the fixed laser intensity, the outward oscillation towards R phase ($A^R(f)$), shown in Fig. S1, cannot increase with f . The eventual decline in $A^R(f)$ may be attributed to a negative feedback effect inherent in the sideways deflection of the experiment. The laser is directed at a point to heat the bimorph in its straight state, and the bimorph absorbs most of the incident laser energy under continuous and low frequency laser operation. At higher frequency operation, the nanobeam spends more time away from the initial state, settling instead in the inward or M2 bending region when the laser is chopped to be off. Consequently, when the laser pulse switches back on, less of the bimorph is in the pathway and less incident energy is absorbed, which reduces the total displacement and heating back towards the R position. It is possible that an alternate experimental setup, with nanobeam oscillation in the plane of the laser beam, could yield high tip displacement performance at even higher frequencies. In this hypothetical setup, the inward (M2) bending is expected first to decline to zero with further inability to cool, followed by the decrease of R-phase bending at high frequencies. Here, the displacement would saturate into the maximum R position. In this regime, the bimorph is unable to cool even to M2 temperatures, and retains the laser-induced R-phase, producing the same displacement that occurs at a continuous laser irradiation. Nonetheless, even given these limitations, the nanobeam bimorphs respond with outward R phase displacements at very high frequencies. From Fig. 4(c), the 3dB-attenuation frequency is 2.5kHz, solely considering outward bending.

Videos of actuation by laser are shown for a 217 μm long bimorph with thickness $\text{VO}_2(1 \mu\text{m})/\text{Cr}(0.3 \mu\text{m})$, and width 1 μm . A low-frequency (10 Hz) chopped laser results in M1-R switching, while high-frequency (2kHz) results in primarily M1-M2, as shown in Movies 3 and 4, respectively.

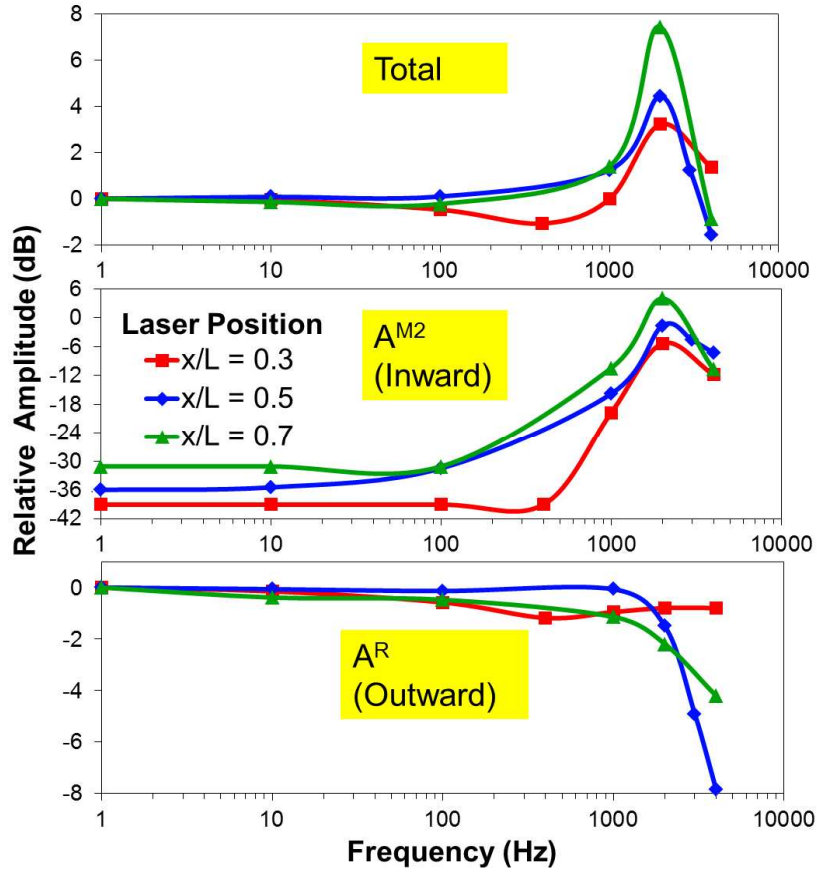


Fig. S1. Decomposition of the total amplitude into M2 amplitude and R amplitude shows the different frequency behavior of the actuation driven by the M1-M2 and M1-R transition. Colored lines are provided as a visual aid. Three laser positions are shown.

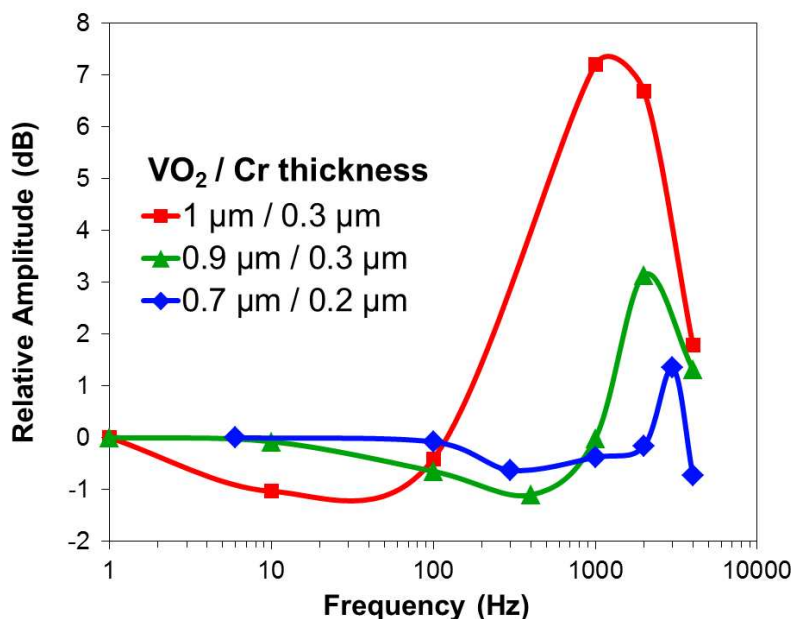


Fig.S2. Frequency response of actuation of 3 cantilevers with different VO₂ thickness. Bimorphs have similar width. Lengths are 100, 115, and 217 μm, respectively. The laser power is fixed for the experiments, and the focal position along the bimorph is fixed at $x/L \sim 0.4$ for all three curves.

5. Self-oscillation (Movie 5).

An intriguing observation is a natural self-oscillation effect: even at un-chopped, continuous laser incidence, a heated bimorph will absorb energy, deflect, cool and then return back towards the laser in a steady, fast cycle. This process can be further studied to shed insight on the heat transfer dynamics. Movie 5 shows this effect for a bimorph of thickness VO₂(1 μm)/Cr(0.3 μm), length 100 μm, and width 1 μm, for an incident laser power of 0.6 mW. By positioning the laser at the nanowire edge opposite to the inward (M2) bending direction, we can verify the negative feedback mechanism observe a natural oscillation in bending. As we move the laser away from its initial position towards the R position, we can induce an increased self-oscillation amplitude. The bimorph increases its R phase deflection and M2 deflection, as it accumulates more heat by coinciding more along the laser beam path.

6. Hybrid bimorph film (Movie 6).

A macroscopic PDMS film with dense and aligned VO₂/Cr bimorphs embedded produced very large actuation amplitudes. Movie 6 shows the response as temperature is varied from 25 °C to 120 °C for a film measuring length 2mm, width 1mm, and thickness 20 μm. The maximum response (amplitude change) occurs in the 70 – 90 °C range, as this temperature at the global heat source results in local temperatures in the film around the phase transition of 68 °C. The bending amplitude ratio was measured to be $A/L = 0.9$, close to but not as high as that in global heating ($A/L = 1.2$) of single bimorphs. There is a small inward bending of the bimorph film as it is heated from 25 °C to 37 °C, indicative of the M2 phase transition.

7. Energy efficiency calculation.

For a linear micro solid engine (μ SE) based on a VO_2 beam oriented along c_R with length L , width a , and thickness b , the maximum energy efficiency can be calculated by

$$\eta_{linear} = \frac{E_{out}}{E_{in}} = \frac{L \cdot \varepsilon_0 \cdot \sigma_C \cdot a \cdot b}{Lab\rho c\Delta T + LabH}, \quad (\text{S1})$$

where ε_0 is the transformation strain (analogous to volume change in the liquid-vapor transition, $\approx 1\%$ for M1-R and 2% for M2-R), σ_C is the critical stress that would drive the phase transition at a given T (analogous to pressure in the liquid-vapor transition, and is the stress at the phase boundary in Fig.S3a), ρ represents density, c the specific heat, and H the latent heat. $\Delta T = T_{MIT} - T_0 = 68^\circ\text{C} - 27^\circ\text{C}$. The numerator in equation (S1) is the work output from a complete engine cycle as shown in Fig.S3a. The Clapeyron equation links σ_C to H ,

$$\frac{d\sigma_C}{dT} = \frac{H}{\varepsilon_0 \cdot T_{MIT}}. \quad (\text{S2})$$

Assuming a linear phase boundary,ⁱⁱ we have

$$\sigma_C = \frac{d\sigma_C}{dT} \cdot \Delta T = \frac{H \cdot \Delta T}{\varepsilon_0 \cdot T_{MIT}}. \quad (\text{S3})$$

Substituting into equation (S1), we obtain

$$\eta_{linear} = \frac{\Delta T}{T_{MIT}} \cdot \frac{1}{1 + \rho c\Delta T/H}. \quad (\text{S4})$$

This is equation (1) in the main text. We note that

$$\eta_{Carnot} = \frac{\Delta T}{T_{MIT}}. \quad (\text{S5})$$

As predicted by equation (S4), although the engine efficiency decreases as T_{low} moves toward $T_{high} = T_{MIT}$, its relative value would approach the Carnot efficiency if the engine is operated near the phase boundary ($\Delta T \rightarrow 0$).

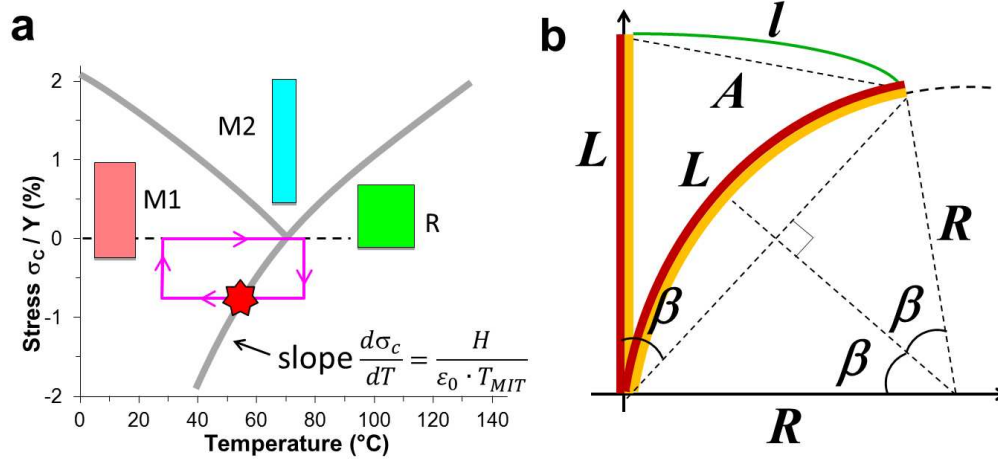


Fig. S3. **a.** The c_R stress – temperature phase diagram of VO₂. The stress is normalized by the Young’s modulus. The Clapeyron equation relates the slope of the phase boundary to the latent heat of transition. The loop shows an engine cycle, where the red star is the point when work is done. **b.** Geometry of the bimorph system for energy efficiency calculation.

For the bimorph μ SE coupling a VO₂ and a Cr layer, the efficiency calculation is more complicated. By treating the bimorph as a bilayer elastic beam with a spring constant, we can estimate the efficiency by dividing the mechanical work output at maximum displacement with the total heat absorbed (global heating). The spring constant is estimated from basic elastic beam theory,ⁱⁱⁱ

$$k_{eff} = \frac{3a}{L^3} \cdot \frac{Y_1^2 b_1^4 + Y_2^2 b_2^4 + 2Y_1 b_1 Y_2 b_2 \cdot (2b_1^2 + 2b_2^2 + 3b_1 b_2)}{12(Y_1 b_1 + Y_2 b_2)}, \quad (S6)$$

where Y is the Young’s modulus ($Y_{VO_2} \approx 140$ GPa and $Y_{Cr} \approx 280$ GPa), L the length, a the width and b the thickness of the beam, and subscript “1” and “2” denote the VO₂ layer and the Cr layer, respectively. Defining the total curved path of the tip motion as l (Fig.S3b), the work output for a full bending cycle is then

$$E_{out} \approx 2 \cdot \frac{1}{2} k_{eff} l^2 \quad (S7)$$

Our system typically operates beyond the “small beam bending” limit, as the displacement is large, $l/L \sim A/L \sim 1$. However, we note that a simple scaling argument predicts the energy efficiency to be an intensive rather than extensive quantity, and be independent of the bimorph length L : a bimorph with length L outputs the same amount of work as two bimorphs each with length $L/2$ connected in series. Therefore, for the efficiency calculation, we only need to calculate for bimorphs with maximum bending still within the linear deformation regime $l/L \ll 1$. This is the case for bimorphs with small L . This is because the bending curvature $1/R$ is generally independent of the beam length L and is given solely by the thicknesses and Young’s moduli of the two layers,^{iv,v}

$$\frac{1}{R} = \frac{6Y_1b_1Y_2b_2(b_1 + b_2)}{Y_1^2b_1^4 + Y_2^2b_2^4 + 2Y_1b_1Y_2b_2 \cdot (2b_1^2 + 2b_2^2 + 3b_1b_2)} \cdot \varepsilon_0, \quad (\text{S8})$$

where ε_0 is the transformation strain. For the Y_1/Y_2 ratio in our case, the largest $1/R$ is given by $b_2/b_1 \approx 0.4$. Comparing bimorphs with the same b_1 and b_2 thicknesses and thus the same $1/R$, those with smaller L give not only smaller l , but also smaller l/L . In fact, it can be proved from the geometry in Fig.S3b that generally,

$$l/L = \int_0^{L/2R} \left| \frac{\sin \beta}{\beta} \right| d\beta. \quad (\text{S9})$$

At small deflection angles (*i.e.*, smaller $L/2R$), we have $l \approx L^2/2R$. Thus we can utilize the bimorph spring constant k_{eff} in the low-deflection Hooke's law behavior given by equation (S7) to predict a work output linearly proportional to L . Since the energy input E_{in} is also proportional to L , the energy efficiency ($\eta = E_{\text{out}}/E_{\text{in}}$) is therefore independent of L . As in the case of linear μSE , the energy input is given by

$$E_{\text{in}} \approx La(b_1\rho_1c_1 + b_2\rho_2c_2)\Delta T + Lab_1H, \quad (\text{S10})$$

where c_1 is the specific heat of VO_2 ($\approx 690 \text{ J/kgK}$),^{vi} c_2 the specific heat of Cr ($\approx 444 \text{ J/kgK}$)^{vii}, and H the latent heat of the MIT of VO_2 ($\approx 1000 \text{ Cal/mol} = 250 \text{ J/cm}^3$).^{viii} A VO_2 density ρ_1 of 4.66 g/cm^3 was used,^{ix} along with a Cr density^x ρ_2 of 7.19 g/cm^3 .

The calculated energy efficiencies are shown in Fig.1d in the main text, for bimorphs with $L = 5 \mu\text{m}$ while varying the thickness. These efficiencies are compared to those of thermoelectrics operating between $T_{\text{high}} = T_{\text{MIT}} = 68 \text{ }^\circ\text{C}$ and $T_{\text{low}} = T_0 = 27 \text{ }^\circ\text{C}$. Assuming the thermoelectric figure-of-merit to be ZT , the thermoelectric engine efficiency is given by,

$$\eta_{\text{TE}} = \frac{T_{\text{high}} - T_{\text{low}}}{T_{\text{high}}} \cdot \frac{\sqrt{1 + ZT} - 1}{\sqrt{1 + ZT} + T_{\text{low}}/T_{\text{high}}}. \quad (\text{S11})$$

We also would like to point out the difference between **intrinsic** energy loss and **extrinsic** energy loss in evaluation of efficiency in an energy conversion technology. Intrinsic loss is the fundamental, unavoidable loss that is attributed to the limit of the working material (such as the thermal conductivity and electrical conductivity of the material in thermoelectrics), while extrinsic loss is the avoidable loss attributed to realistic limit in a device design (such as the heat loss via air or packaging material, and energy loss due to contact resistance in thermoelectrics). Without the intrinsic loss, the efficiency would approach the Carnot efficiency. Without the extrinsic loss, the efficiency of thermoelectrics will be given by Eq.(S11).

In analogy, in our efficiency evaluation of $\text{VO}_2 \mu\text{SE}$, the intrinsic energy loss is indeed included, which is the heat needed to increase the VO_2 temperature up to the MIT temperature (determined by the specific heat of VO_2 , and completely lost during a cycle). Without this intrinsic loss term, the efficiency will be simply the Carnot efficiency. The extrinsic energy loss is the loss via air convection, or possible friction loss during actuation. Without the extrinsic loss, the efficiency is given Eq.(S4).

Therefore, to analyze the pure materials performance in the VO₂ engine, we believe it is indeed a fair and appropriate comparison, to compare the intrinsic efficiency predicted by Eq.(S4) in our case, to the intrinsic efficiency predicted by Eq.(S11) in the case of thermoelectrics. The following table summarizes the different levels of efficiency calculation between these two mechanisms.

Mechanism		Thermoelectrics	VO ₂ for actuation (this work)
Physical limit	Condition	$\kappa = 0, \sigma = \infty, ZT = \infty$	$c = 0, H = \infty$
	Efficiency	$\eta = \eta_{\text{Carnot}}$	$\eta = \eta_{\text{Carnot}}$
Materials limit (Only intrinsic loss included)	Condition	$\kappa > 0, \sigma < \infty, ZT$ finite. Intrinsic loss: heat conduction, Joule heat.	$c > 0, H < \infty$. Intrinsic loss: heat capacity.
	Efficiency	$\eta < \eta_{\text{Carnot}}$; $\eta = 3.4\%$ for $ZT = 2.1$	$\eta < \eta_{\text{Carnot}}$; $\eta = 3.4\%$ for c and H of VO ₂
device limit (Extrinsic loss also included)	Condition	Additional extrinsic loss: air heat loss, contact resistance loss, etc.	Additional extrinsic loss: air heat loss, friction loss, etc.
	Efficiency	$\eta < 3.4\%$ for $ZT = 2.1$	$\eta < 3.4\%$ for c and H of VO ₂

8. Calculation of cantilever resonant frequency

From beam theory, we know the spring constant for a simple beam in transverse oscillation^{xi} is given by

$$k = \frac{F}{\delta} = \frac{3EI}{L^3} \quad (\text{S12})$$

forming the general case of equation (S7), where the bending modulus (stiffness) EI is replaced by the expression for a bimorph. We find the resonant frequency f_n with the relation

$$f_n = \frac{1}{2\pi} \sqrt{\frac{k}{m_{\text{eff}}}} \quad (\text{S13})$$

where $m_{\text{eff}} = \frac{33}{140}m = \frac{33}{140}\rho abL$ is used, since the beam mass is distributed (resulting in varying velocities) along the oscillation length. For a beam sharing the dimensions in our experiment and the frequency calculations of thermal transport in the main text ($L = 150 \mu\text{m}$, $a = 700\text{nm}$, $b_1 = 700\text{nm}$, $b_2 = 200\text{nm}$), the resonant frequency is calculated to be 1.29 MHz, significantly higher than the frequencies examined by pulsed optical excitation. Thus the rise in deflection amplitudes at intermediate frequencies is not attributed to resonance, but rather the M2-R transition.

-
- ⁱ Rua, A.; Cabrera, R.; Coy, H.; Merced, E.; Sepulveda, N.; Fernandez, F. E. Phase Transition Behavior in Microcantilevers Coated with M₁-phase VO₂ and M₂-phase VO₂:Cr Thin Films. *J. Appl. Phys.* **2012**, *111*, 104502.
- ⁱⁱ Cao, J.; Gu, Y.; Fan, W.; Chen, L. Q.; Ogletree, D. F.; Chen, K.; Tamura, N.; Kunz, M.; Barrett, C.; Seidel, J. *et al.* Extended Mapping and Exploration of the Vanadium Dioxide Stress-Temperature Phase Diagram. *Nano Lett.* **2010**, *10*, 2667–2673.
- ⁱⁱⁱ Shen, D.; Park, J.-H.; Ajitsaria, J.; Choe, S.-Y.; Wickle, H. C.; Kim, D.-J. The Design, Fabrication and Evaluation of a MEMS PZT Cantilever with an Integrated Si Proof Mass for Vibration Energy Harvesting. *J. Micromech. Microeng.* **2008**, *18*, 055017.
- ^{iv} Cao, J.; Fan, W.; Zhou, Q.; Sheu, E.; Liu, A.; Barrett, C.; Wu, J. Colossal Thermal-mechanical Actuation via Phase Transition in Single-crystal VO₂ Microcantilevers. *J. Appl. Phys.* **2010**, *108*, 083538.
- ^v Timoshenko, S. Analysis of Bi-Metal Thermostats. *J. Opt. Soc. Am.* **1925**, *11*, 233–255.
- ^{vi} Berglund, C. N.; Guggenheim, H. J. Electronic Properties of VO₂ Near the Semiconductor-Metal Transition. *Phys. Rev.* **1969**, *185*, 1022–1033.
- ^{vii} Williams, I. S.; Gopal, E. S. R.; Street, R. The Specific Heat of Strained and Annealed Chromium. *Journal of Physics F: Metal Physics* **1979**, *9*, 431–445.
- ^{viii} Cao, J.; Ertekin, E.; Srinivasan, V.; Fan, W.; Huang, S.; Zheng, H.; Yim, J. W. L.; Khanal, D. R.; Ogletree, D. F.; Grossman, J. C. *et al.* Strain Engineering and One-dimensional Organization of Metal-insulator Domains in Single-crystal Vanadium Dioxide Beams. *Nature Nanotech.* **2009**, *4*, 732–737.
- ^{ix} McWhan, D. B.; Marezio, M.; Remeika, J. P.; Dernier, P. D. X-ray Diffraction Study of Metallic VO₂. *Phys. Rev. B* **1974**, *10*, 490–495.
- ^x Straumanis, M. E.; Weng, C. C. The Precise Lattice Constant and the Expansion Coefficient of Chromium Between +10 and +60° C. *Acta Crystallographica* **1955**, *8*, 367–371.
- ^{xi} Stokey, W. F. Vibration of Systems Having Distributed Mass and Elasticity. In *Shock and Vibration Handbook*; Harris, C.M., Crede, C.E., Eds.; McGraw-Hill: New York, 1976), pp 7.1 – 7.18